Statistical homogenization of elastic properties of cement paste based on X-ray microtomography images

J. Huang *, K. Krabbenhoft, A.V. Lyamin

ARC Centre of Excellence for Geotechnical Science and Engineering, Priority Centre for Geotechnical and Materials Modelling, Civil, Surveying and Environmental Engineering, The University of Newcastle, Callaghan, NSW 2308, Australia

ARTICLE INFO

ABSTRACT

This paper proposes a statistical multiscale homogenization method to extract effective elastic properties of cement paste on the basis of X-ray microtomography images. The procedure starts at the nanolevel of the C-S-H matrix. Because the highest resolution of current X-ray microtomography is at micrometer scale, C-S-H and CH remains unsegmented. The unresolved hydrated cement is homogenized by a two-step analytical method based on Mori–Tanaka (M–T) scheme. A statistical numerical homogenization method based on the Finite Element Method (FEM) was used to homogenize the elastic properties of cement pastes. Mean elastic properties showed good agreement with experimental results. The proposed multiscale method combines advanced analytical, numerical and experimental methods in a systematical way so that the inputs are phase material properties and X-ray microtomography images only. The novelty of this method is in the avoidance of any subjective decision.

© 2012 Elsevier Ltd. All rights reserved.

1. Introduction

To build a realistic homogenization model, a detailed investigation of microstructure is primarily required. In particular, we need to specify the involved phases and their mechanical properties, distributions, sizes and shapes. In the case of cement paste, the microstructure developed by hydration is extremely complex and still subject to numerous investigations. In the hydration reaction, anhydrous cement grains react with water to produce hydrates, and in the process increase the solid volume of the system. This additional solid bridges the spaces between grains, leading to the formation of a solid mass. In Portland cement paste, the hydration reaction is dominated by the reaction of the tricalcium silicate (C_3S), which produces calcium hydroxide (CH) and calcium silicate hydrate (C-S-H). The deposition of these phases in the microstructure is quite distinct. CH deposits dominantly in the pore space, but is engulfed with processing C-S-H. The existence of two types of C-S-H appears nowadays as a well-established fact in cement chemistry. Jennings (2000) and Tennis and Jennings (2000) classified them as high-density and low density, whereas Richardson (2000) preferred to call them inner and outer products. In this paper, the high and low density C-S-H are denoted by C-S-H$_H$ and C-S-H$_L$, respectively. More recently, nanoscale CH crystals were found in the C-S-H of low w/c ratio cement paste (Chen et al., 2010). The Young's moduli of C-S-H$_H$ and C-S-H$_L$ obtained by nan-oindentation showed independence of water/cement ratio, admixtures, etc. This suggests that the properties are intrinsic to all types of cement-based materials (Constantinides and Ulm, 2004), making it possible to estimate the elastic properties of various cement pastes within a single framework.

The pore size of cement paste ranges from a few nanometres to tens of micrometers and can be divided into intra-solid pores, gel pores and capillary pores. Jennings (2000) and Tennis and Jennings (2000) provided qualitative and quantitative evidence of an amorphous colloidal structure of the C-S-H, composed of basic building blocks and an intra-globules porosity of 18%. This porosity is irrespective of the type of C-S-H. The difference between the two types of C-S-H relates to the gel porosity of roughly 24% for C-S-H$_H$, and 37% for C-S-H$_L$ (Jennings, 2000), due to the different packing density of the C-S-H solid of the two types of C-S-H. Capillary pores correspond to the originally water filled spaces not filled by hydration products.

A few experimental techniques, such as X-ray microtomography (Bentz et al., 2002) and focused ion beam nanotomography (Holzer et al., 2006; Munch et al., 2006; Trtik et al., 2009, 2011) have been attempted to finely resolve the 3-D pore/solid structure of cement paste. The detailed distribution of phases, however, is often difficult to obtain because it involves a specification of the phase that is present at each point in space (Jennings et al., 2008). Research in this field is still underway.

Despite its complex microstructure, attempts to investigate the mechanical properties of cement paste have never ceased, because concrete is by far the most used material in construction engineer-

* Corresponding author. Tel.: +61 02 49215118; fax: +61 02 49216946.
  E-mail address: jinsong.huang@newcastle.edu.au (J. Huang).

ing. Young's modulus (E) and Poisson's ratio (v) are important parameters used in structural design and the analyses of cement-based materials. Experimental tests, analytical estimates and numerical homogenizations are typical methods to obtain the elastic properties of cement paste. Although experimental tests are usually thought of as reliable methods, there are relatively fewer tests (e.g., Boumiz et al., 1996; Sun et al., 2005) on cement paste than other materials such as concrete, rock and soil.

Analytical estimates are based on micromechanics homogenization theories. The M–T scheme (Mori and Tanaka, 1973), the self-consistent (SC) scheme (Hill, 1965) and the interaction direct derivative (IDD) scheme (Zheng and Du, 2001) are commonly used for the homogenization of cementitious material. An efficient micromechanical homogenization procedure, which starts at the nanolevel of the C-S-H matrix, has been developed by Constantinides and Ulm (2004). Estimated Young's moduli for both sound and leached ordinary Portland cement pastes with water/cement mass ratio ($w/c = 0.5$) showed good agreement with experimental results. Bernard et al. (2003) used the same two-scale description of microstructure and the SC scheme to study early-age cement pastes and predict the solid phase percolation during hydration process and results consistent with experimental values were obtained. The SC scheme with spheroids was used by Sanahuja et al. (2007) to predict the elastic properties of hydrating cement paste. It was assumed that anhydrous grains surrounded by a layer of inner phase (C-S-H$_H$) are embedded in an outer matrix (C-S-H$_L$). The Jennings–Tennis model (Jennings, 2000; Tennis and Jennings, 2000) was used to get the volume fractions of C-S-H$_H$ and C-S-H$_L$.

The numerical homogenization needs a description of the microstructure of material. Three types of methods are commonly used to obtain the microstructure of cement paste. They are numerical generations, numerical simulations and X-ray microtomography. The numerical generation approach has been adopted by Stefan et al. (2010) and Bary et al. (2009). A burning algorithm was used by Stefan et al. (2010) to model the setting phenomenon of cement paste. A percolated cluster was obtained and the FEM calculation approach was applied to predict the material mechanical properties with time. Bary et al. (2009) compared the performance of several effective medium approximation schemes (M–T, SC, IDD) through their ability to estimate the mechanical properties of cement paste. Several samples were obtained by numerical generation and three dimensional FEM was used to homogenize their elastic properties.

Garboczi et al. (2004) and Haecker et al. (2005) used the NIST cement hydration model (Bentz, 1997) and a three dimensional FEM to predict the elastic properties of Portland cement paste. The required individual phase moduli were adopted from the literature. Experimental tests were also carried out and their comparison with the results obtained by elastic finite element calculations showed a good agreement for degrees of hydration above 0.5. Instead of using numerical homogenization, Smilauer and Bittnar (2006) presented a combination of the NIST cement hydration model and the analytical homogenization approach.

The combination of recent advances in X-ray microtomography together with numerical simulations based on the FEM have led to a powerful new tool for estimating the properties of porous materials, particularly their elastic properties. Madadi et al. (2009) describes a wide range of potential applications of this technology for estimating the elastic properties of porous materials (ideal granular packing, sphere pack, sandstones, carbonates, bone sample and fracture sample). Arns et al. (2002) calculated the elastic properties of a tomographic image of sandstone. The elastic properties of the digitized images under dry, water-saturated, and oil-saturated conditions were considered. The obtained numerical predictions were in excellent agreement with available experimental data. Fontainebleau sandstone was chosen because it is made

up of a single mineral (quartz) and does not contain clay. Also the structure of the sandstone is quite simple as it only displays intergranular porosity. Modeling the system as a simple two-phase material may be expected to provide a good match to experimental data. Such approaches have been applied in homogenizations of cement paste in recent years. Wriggers and Hain (2007) and Hain and Wriggers (2008) used three-dimensional X-ray microtomography combined with FEM based numerical homogenization techniques to study effective elastic properties of hardened cement paste. Statistical tests, two- and three-dimensional computations and a comparison with experimental data have been presented. The two types of C-S-H were not considered. Krabbenhoft et al. (2008) and Karim and Krabbenhoft (2010) considered the effective diffusivities of cement paste on the basis of X-ray microtomography images. A general computational homogenization framework was developed and applied to a variety of cement pastes whose microstructure has been digitized to a resolution of $0.95^3 \mu m^3$ (Bentz et al., 2002). However, at this resolution, important submicron features are not resolved. Consequently, a simple rule that incorporates microtomography data was proposed and shown to yield satisfactory results (Karim and Krabbenhoft, 2010).

The NIST Visual Cement Data Set (Bentz et al., 2002) was obtained at a resolution of $0.95^3 \mu m^3$. As mentioned previously, a detailed phase segmentation cannot be done at such a resolution. For example, it is impossible to distinguish the two types of calcium silicate hydrate (C-S-H). In order to use the NIST Visual Cement Data Set to predict elasticity properties, a multiscale statistical method is proposed in this paper. The image of cement paste is segmented into three phases: (1) pores larger than $0.95^3 \mu m^3$, (2) hydrated cement, and (3) unhydrated cement. This segmentation approach avoids any subjective decision as will be discussed later. The unresolved hydrated cement that consists of C-S-H$_H$, C-S-H$_L$, CH and pores smaller than $0.95^3 \mu m^3$, is homogenized by the two-step homogenization scheme developed by Constantinides and Ulm (2004). A statistical numerical homogenization method based on the FEM was used to estimate the effective elastic properties of cement paste. Results obtained for degrees of hydration above 0.4 showed good agreement with experimental data. The inputs for the method presented in this paper are phase material properties and X-ray microtomography images only. This avoids any subjective decision and differs from previous work.

2. Data segmentation

2.1. Materials and X-ray microtomography data

In the current study, the NIST Visible Cement Data Set was used. Cement paste specimens were prepared from the Cement and Concrete Reference Laboratory (CCRL) cement 133, issued in June of 1999. Complete information on this cement can be found in the NIST Cement Images database. The volume fractions of the four chief minerals of cement 133 are listed in Table 1.

Cement pastes with water/cement mass ratios (w/c) between 0.3 and 0.45 were prepared and viewed after various hydration times. After drill mixing in a plastic beaker, small parts of the paste were 'extruded' into circular tube molds with an internal diameter of 1 mm. Subsequently, the whole assembly was scanned at a resolution of $0.95^3 \mu m^3$, and reconstructed three-dimensional data sets containing 1024^3 voxels (volume pixels) were obtained. From

Table 1
Cement 133.

Cement	ϕ_{C_3S}	ϕ_{C_2S}	ϕ_{C_3A}	ϕ_{C_4AF}
CCRL cement 133 (June 1999)	0.7018	0.1315	0.0827	0.0840

these data sets, smaller volumes consisting of 300^3 voxels were extracted. These data form the basis of the homogenization conducted in the current study. In order to illustrate the procedures developed, in the following we will use a particular data set (pt045_sld_7dv1c300), which describes the microstructure of a cement paste with an initial water/cement mass ratio of $w/c = 0.45$ and a hydration time of 137 h.

2.2. Segmentation

Standard X-ray microtomography images comprise grayscale maps with values proportional to the linear attenuation coefficient at each material point. Typically, the data is organized as a collection of cubic volume elements (voxels), each of which is assigned a unique grayscale value. Next, the data are segmented into a number of distinct categories corresponding to distinct material phases. In the current study, the segmentation is based on the frequency distribution of the grayscale count (e.g., Bentz et al., 2002). This distribution is shown in Fig. 1. From this plot, several distinct peaks are evident. First, approximately 6.7% of the voxels have a grayscale value of $T = 0$. This corresponds to air and water filled pores that are larger than 0.95^3 μm^3 ($\phi_{p>0.95^3 \ \mu m^3} = 0.067$). Secondly, two peaks, at grayscale values of $T = 60$ and $T = 130$ are visible. These peaks are associated with hydrated and unhydrated cement, respectively. It is not possible to further separate the hydrated cement into C-S-H, CH and pores smaller than 0.95^3 μm^3 without any subjective decision. It is thus proposed herein that the cement paste is separated into three phases: pores larger than 0.95^3 μm^3, hydrated cement and unhydrated cement. A threshold of $T_{hu} = 114$, corresponding the lowest point in the valley between the two peaks (see Fig. 1) is first chosen. The voxels that have grayscale values larger than T_{hu} are treated as unhydrated cement. The voxels that have grayscale values smaller than T_{hu}, but larger than zero, are treated as unhydrated cement. The hydrated cement consists of C-S-H$_H$, C-S-H$_L$, CH and pores smaller than 0.95^3 μm^3. An example of a slice from the data set at this level of thresholding is shown in Fig. 2. From the individual slices, the full three-dimensional volume may be reconstructed. An example of a 300^3 volume is shown in Fig. 3.

The volume fractions of the three separated phases are estimated by the classic Powers hydration model (Power, 1962). Although it was introduced back in the 40s, the Powers hydration

model remains widely used because of its reliability and the ease of implementation. This model includes the following predictions of volume fractions of capillary pores and unhydrated cement paste on the basis of the initial water/cement mass ratio and the current degree of hydration:

$$\phi_p = \frac{w/c - 0.36\alpha}{w/c + 0.32}$$
$$\phi_u = \frac{0.32(1 - \alpha)}{w/c + 0.32} \qquad (1)$$
$$\phi_h + \phi_u + \phi_p = 1$$

where w/c is the water/cement mass ratio, α is the degree of hydration, ϕ_h, ϕ_u and ϕ_p are the volume fractions of the hydrated, unhydrated and (capillary) pore, respectively. First, ϕ_u is estimated by dividing the number of voxels that have grayscale values larger than $T_{hu} = 114$ by the total number of voxels. This gives a value of $\phi_u = 0.154$, resulting in $\alpha = 0.63$. Finally, this degree of hydration, together with the water/cement mass ratio of $w/c = 0.45$ gives a porosity of $\phi_p = 0.290$. This porosity is the total capillary porosity consisting of pores larger or smaller than 0.95^3 μm^3.

Seven data sets of cement pastes were selected to be homogenized in this paper. They were selected because there is an obvious valley (or T_{hu} value) in their frequency distributions of the grayscale count. The homogenization of cement pastes without such valleys is worth further investigations.

The water cement mass ratio (w/c), the volume fraction of pores larger than 0.95^3 μm^3 ($\phi_{p>0.95^3 \ \mu m^3}$), the grayscale value that separates hydrated and unhydrated cement (T_{hu}), the volume fraction of unhydrated cement (ϕ_u), the degree of hydration (α) and the capillary porosity (ϕ_p) of the seven selected data sets are summarized in Table 2.

3. Two-step homogenization of hydrated cement

Although elastic properties of all the main phases present in cement paste are measurable by nanoindentation techniques and many data may be found in the literature, it is not possible to use them directly in the numerical homogenizations based on X-ray microtomography images. This is because the resolution of microtomography is 0.95^3 μm^3, individual phases remain undistinguished. In the present study, the two-step homogenization procedure developed by Constantinides and Ulm (2004) is adopted for the homogenization of the unresolved hydrated cement. The first step is applied to the C-S-H matrix consisting of two types of C-S-H at a scale of nanometres. The volume fractions of the two types of C-S-H are obtained based on Jennings–Tennis model. The second step is applied to the hydrated cement, which consists of the homogenized medium (C-S-H matrix) of step one, CH and pores smaller than 0.95^3 μm^3. The volume fractions of C-S-H and CH are obtained by stoichiometric calculations. The M–T scheme is used in both steps and individual phase properties are nanoindentation results found in the literature.

3.1. Step I

At step I, the C-S-H matrix behaves as a heterogeneous material with an inclusion-matrix type microstructure. The C-S-H$_L$ plays the role of a matrix phase, surrounding the C-S-H$_H$ as inclusion. The M–T scheme needs as input the volume fractions of two types of C-S-H. Jennings (2000) and Tennis and Jennings (2000) proposed a quantitative model of the distribution of C-S-H$_H$ and C-S-H$_L$. An estimate of the ratio of the mass of low density to the total mass of C-S-H is given by (in dried conditions):

$$m_{LD} = 3.017\alpha w/c - 1.347\alpha + 0.538 \qquad (2)$$

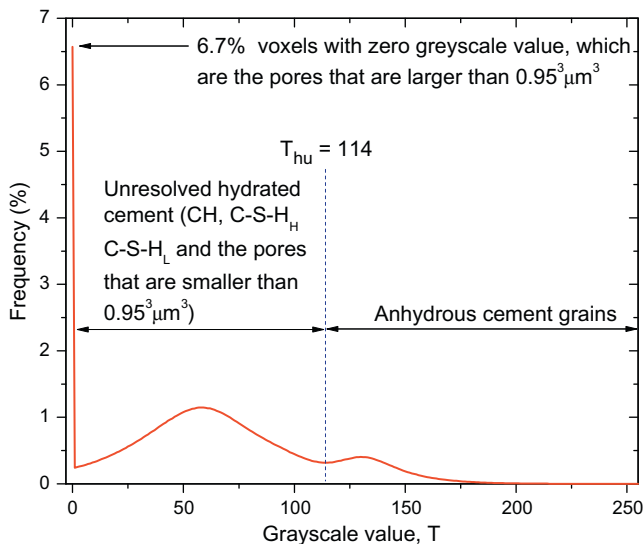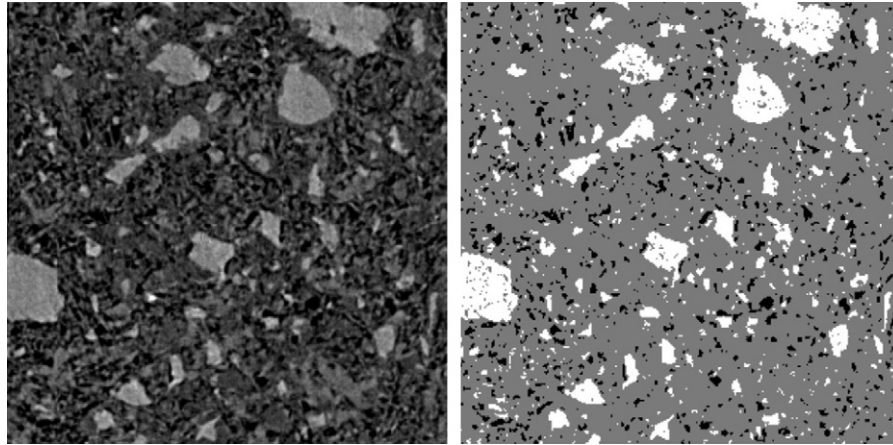**Fig. 1.** Grayscale level frequency distribution.

Fig. 2. Micro-CT slices of the cement paste at a resolution of 0.95^3 μm³. Each slice consists of $300 \times 300 \times 1$ voxels. The left panel shows the original grayscale data and the right panel shows the result of thresholding into three phases: pores larger than 0.95^3 μm³ (dark), the hydrated cement (grey) and the unhydrated cement (white).

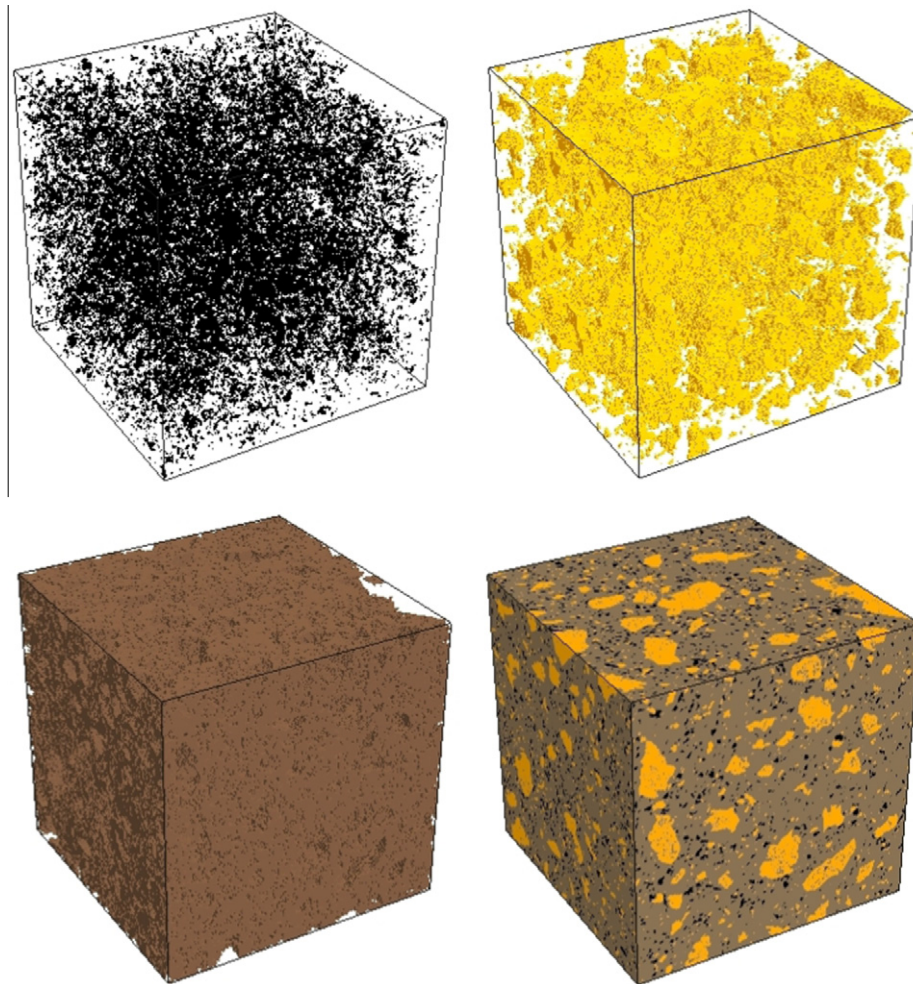**Fig. 3.** Three-dimensional reconstruction of the cement paste: pores larger than 0.95^3 μm³ (top left), the unhydrated (top right), the hydrated (bottom left), and the combined cement paste (bottom right). The combined volume consists of $300^3 = 27,000,000$ voxels, each of which is represented by an 8-node finite element.

By using the mass densities in Table 3, the mass fraction m_{LD} can be directly converted into the volume fraction ϕ_{LD}:

$$\phi_{LD} = \frac{m_{LD}\rho_{HD}}{\rho_{LD} + m_{LD}(\rho_{HD} - \rho_{LD})} \qquad (3)$$

The volume fractions of C-S-H$_L$ (ϕ_{LD}) of the seven selected data sets are listed in Table 5. By using the M–T scheme and the properties of individual phases listed in Table 4, the mass densities and elastic properties of C-S-H are obtained and listed in Table 5. Also listed in Table 4 are the elastic properties of anhydrous to be used

Table 2
Seven data sets selected from the NIST Visible Cement Data Set.

Data set		w/c	$\phi_{p>0.95^3\ \mu m^3}$	T_{hu}	ϕ_u	α	ϕ_p
1	pate03_1_52hv1c300	0.3	0.021	114	0.293	0.432	0.233
2	pt03_spr_2mmv1c300	0.3	0.0003	162	0.252	0.512	0.187
3	p35h40v1c300	0.35	0.082	117	0.261	0.462	0.283
4	cez16_sld_2mmv1c300	0.40	0.021	151	0.087	0.805	0.157
5	cez16_d_6dv1c300	0.40	0.042	112	0.138	0.696	0.222
6	pt045_sld_2mmv1c300	0.45	0.032	142	0.110	0.745	0.245
7	pt045_sld_7dv1c300	0.45	0.066	114	0.154	0.637	0.288

Table 3
Mass densities of C-S-H$_L$ and C-S-H$_H$.

Phase	ρ (kg/m^3)	References
C-S-H$_L$	1700	Jennings et al. (2007) and Ulm et al. (2007)
C-S-H$_H$	2000	Jennings et al. (2007) and Ulm et al. (2007)

Table 4
Elastic properties of phases.

Phase	E (GPa)	v	References
C-S-H$_L$	21.7	0.24	Constantinides and Ulm (2004)
C-S-H$_H$	29.4	0.24	Constantinides and Ulm (2004)
CH	38	0.31	Bernard et al. (2003) and Constantinides and Ulm (2004)
Anhydrous	135	0.3	Sanahuja et al. (2007) and Stefan et al. (2010)

Table 5
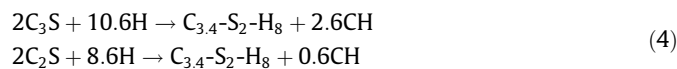Homogenized properties of C-S-H matrix.

Data set	ϕ_{LD}	ρ_{C-S-H} (kg/m^3)	$E_{C-S-H}^{(M-T)}$ (GPa)	$v_{C-S-H}^{(M-T)}$
1	0.385	1884.57	26.13	0.24
2	0.348	1895.71	26.43	0.24
3	0.443	1867.04	25.67	0.24
4	0.465	1860.42	25.50	0.24
5	0.481	1855.77	25.38	0.24
6	0.586	1824.25	24.59	0.24
7	0.585	1824.59	24.60	0.24

later in the homogenizations of cement paste. For the sake of simplicity, the elastic properties of C$_3$S were used for all of the clinker phases (e.g., Haecker et al., 2005) in the computations reported in this paper.

3.2. Step II

At step II, the main phases are the homogenized C-S-H, CH and pores smaller than 0.95^3 μm^3. Precisely, the C-S-H acts as a matrix phase in which the other phases are embedded and play the role of inclusion.

The two chemical equations that define the quantity of C-S-H formed are (e.g., Tennis and Jennings, 2000)

$$2C_3S + 10.6H \rightarrow C_{3.4}\text{-}S_2\text{-}H_8 + 2.6CH$$
$$2C_2S + 8.6H \rightarrow C_{3.4}\text{-}S_2\text{-}H_8 + 0.6CH \tag{4}$$

In order to determine the volume fractions of C-S-H and CH, the hydration kinetics model may be used to determine the hydration degree of each clinker phase (Bernard et al., 2003). For ordinary Portland cement, by taking only C$_3$S into account, the amounts of C-S-H and CH can be simply related (e.g., Eijk van and Brouwers,

Table 6
Mass densities of phases.

Phase	ρ (kg/m^3)	References
C$_3$S	3150	Taylor (1997)
C$_2$S	3280	Taylor (1997)
CH	2240	Taylor (1997)

1998). In the present study, both C$_3$S and C$_2$S are taken into account. It is assumed however, that C$_3$S and C$_2$S have a same clinker degree of hydration α_c.

The numbers of moles of C$_3$S and C$_2$S per unit volume of cement are given by

$$M_{C_3S} = \frac{\phi_{C_3S}\rho_{C_3S}}{\mathfrak{M}_{C_3S}}$$
$$M_{C_2S} = \frac{\phi_{C_2S}\rho_{C_2S}}{\mathfrak{M}_{C_2S}} \tag{5}$$

where ρ_{C_3S} and ρ_{C_2S} are the mass densities of C$_3$S and C$_2$S as listed in Table 6, $\mathfrak{M}_{C_3S}$ and $\mathfrak{M}_{C_2S}$ are the molar mass of C$_3$S and C$_2$S as listed in Table 7.

Based on Eq. (4), the numbers of moles of C-S-H and CH formed from one unit volume of cement, are given by

$$M_{C-S-H} = \alpha_c(M_{C_3S} + M_{C_2S})$$
$$M_{CH} = \alpha_c(1.3M_{C_3S} + 0.3M_{C_2S}) \tag{6}$$

The volumes of C-S-H and CH are thus obtained as

$$V_{C-S-H} = \frac{M_{C-S-H}\mathfrak{M}_{C-S-H}}{\rho_{C-S-H}}$$
$$V_{CH} = \frac{M_{CH}\mathfrak{M}_{CH}}{\rho_{CH}} \tag{7}$$

where ρ_{CH} is the mass density of CH as listed in Table 6, ρ_{C-S-H} is the mass density of C-S-H computed by step I (Table 5), $\mathfrak{M}_{C-S-H}$ and $\mathfrak{M}_{CH}$ are the molar mass of C-S-H and CH as listed in Table 7.

The volume fractions of the three phases are given by

$$\phi_{p<0.95^3\ \mu m^3}^h = \frac{\phi_{p<0.95^3\ \mu m^3}}{\phi_h + \phi_{p<0.95^3\ \mu m^3}}$$
$$\phi_{C-S-H}^h = \left(1 - \phi_{p<0.95^3\ \mu m^3}^h\right)\frac{V_{C-S-H}}{V_{C-S-H} + V_{CH}} \tag{8}$$
$$\phi_{CH}^h = \left(1 - \phi_{p<0.95^3\ \mu m^3}^h\right)\frac{V_{CH}}{V_{C-S-H} + V_{CH}}$$

where $\phi_h = 1 - \phi_p - \phi_u$, $\phi_{p<0.95^3\ \mu m^3} = \phi_p - \phi_{p>0.95^3\ \mu m^3}$, ϕ_p and ϕ_u have been obtained as listed in Table 2, the superscript h indicates that the volume fraction is calculated at the level of hydrated cement, $\phi_{p<0.95^3\ \mu m^3}^h$ is the volume fraction of pores smaller than 0.95^3 μm^3, ϕ_{CH}^h is the volume fraction of CH and ϕ_{C-S-H}^h is the volume fraction of C-S-H.

By using the M–T scheme, the elastic properties of hydrated cement are obtained and listed in Table 8.

Table 7
Molar mass of phases.

Phase	$\mathfrak{M}$ (g/mol)	References
C$_3$S	228.32	Bernard et al. (2003)
C$_2$S	172.24	Bernard et al. (2003)
C-S-H	227.2	Bernard et al. (2003)
CH	74	Bernard et al. (2003)

4. Analytical homogenization of cement paste

After the volume relation between C-S-H and CH has been obtained, it is ready to homogenize directly the elastic properties of cement paste based on the M–T scheme. For the sake of simplicity, and because it still correctly captures the main features of the pore structure, cement paste can be thought of as consisting of anhydrous cement grains, CH, C-S-H and pores. It is assumed again that the C-S-H acts as a matrix phase and the other three phases play the role of inclusion.

The volume fractions of C-S-H and CH at the level of cement paste are given by

$$\phi_{\text{C-S-H}} = (1 - \phi_{\text{p}} - \phi_{\text{u}})\frac{V_{\text{C-S-H}}}{V_{\text{C-S-H}} + V_{\text{CH}}} \tag{9}$$

$$\phi_{\text{CH}} = (1 - \phi_{\text{p}} - \phi_{\text{u}})\frac{V_{\text{CH}}}{V_{\text{C-S-H}} + V_{\text{CH}}} \tag{10}$$

where $V_{\text{C-S-H}}$ and V_{CH} are obtained using Eq. (7), ϕ_{p} and ϕ_{u} have been obtained as listed in Table 2.

The input elastic properties of anhydrous cement grains, CH and C-S-H are listed in Tables 4 and 5. The volume fractions of the four phases and the homogenized properties of cement paste are summarized in Table 9. Also listed in Table 9 are the shear moduli, which will be used later to compare with experimental results. The shear modulus is calculated as

$$G = \frac{E}{2(1 + \nu)} \tag{11}$$

5. Statistical homogenization of cement paste

In order to study the effect of the random microstructure of cement paste on its overall elastic properties, a statistical numerical homogenization method based on X-ray microtomography images has been developed. In this approach, each voxel of the X-ray microtomography images is treated as an eight-node finite element. It should be mentioned that finer mesh has been attempted which gave slightly different homogenized properties, but the difference never exceeded two percent. The three phases considered are anhydrous cement grains, hydrated cement and pores larger than $0.95^3\ \mu\text{m}^3$. The elements are assigned the physical properties by their grayscale values and the segmentation method presented in Section 2. The elastic properties of anhydrous cement grains listed

Table 8
Homogenized properties of hydrated cement.

Data set	$\phi_{\text{p}<0.95^3\ \mu\text{m}^3}^{\text{h}}$	$\phi_{\text{C-S-H}}^{\text{h}}$	$\phi_{\text{CH}}^{\text{h}}$	$E_{\text{h}}^{\text{(M–T)}}$ (GPa)	$\nu_{\text{h}}^{\text{(M–T)}}$
1	0.309	0.532	0.160	14.72	0.24
2	0.250	0.576	0.174	16.94	0.24
3	0.305	0.535	0.159	14.60	0.24
4	0.152	0.654	0.194	20.27	0.25
5	0.196	0.620	0.183	17.48	0.24
6	0.249	0.582	0.170	15.97	0.24
7	0.285	0.554	0.161	14.73	0.24

Table 9
Homogenized properties of cement pastes based on the M–T scheme.

Data set	ϕ_{p}	$\phi_{\text{C-S-H}}$	ϕ_{CH}	ϕ_{u}	$E^{\text{(M–T)}}$ (GPa)	$\nu^{\text{(M–T)}}$	$G^{\text{(M–T)}}$ (GPa)
1	0.233	0.365	0.109	0.293	25.34	0.24	10.22
2	0.187	0.431	0.130	0.252	26.72	0.24	10.77
3	0.283	0.352	0.104	0.261	21.61	0.24	8.71
4	0.157	0.584	0.173	0.087	22.44	0.25	8.98
5	0.222	0.494	0.146	0.138	20.81	0.24	8.39
6	0.245	0.500	0.145	0.110	18.78	0.25	7.51
7	0.288	0.432	0.126	0.154	18.14	0.25	7.26

in Table 4 were used. For hydrated cement its homogenized properties have been obtained by the two-step M–T scheme (Table 8). A small value of 0.001 was assigned to the Young's modulus and Poisson's ratio of pores.

If the effective material behavior is assumed to be of a general elastic type, it is necessary to find 21 independent effective material coefficients. These entries can be evaluated if six independent loadings are applied to the RVE. In the current study, it is assumed that the elastic properties of cement pastes are linear and isotropic (Haecker et al., 2005).

5.1. Finite element model

Orthogonal-mixed boundary conditions shown in Fig. 4 were used. Such boundary conditions were proposed by Hazanov and Huet (1994), Hazanov and Amieur (1995) and Khisaeva and Ostoja-Starzewski (2006) and have been used in homogenization of elastic properties of cement paste (e.g., Stefan et al., 2010) and other materials (e.g., Kenesei et al., 2004; Iuga and Raether, 2007). Hazanov (1998) showed that such boundary conditions can only be used for materials having at least orthotropic elastic symmetry properties. For anisotropic materials, periodic boundary conditions are usually used, but this is not necessary unless the microstructures are periodic (Garboczi and Day, 1995).

At the bottom and the two back faces of the RVE, the displacements perpendicular to the respective faces are fixed. A special tied freedom boundary condition is applied on the top and the two front faces so that the displacements perpendicular to the respective faces are constrained to be equal. The nodes of all six faces are free to move in the directions parallel to the respective faces. A unit vertical force shown as the red[1] arrow in Fig. 4 is applied to the tied vertical degrees-of-freedom on the top of the specimen. These boundary conditions ensure that no matter what degree of heterogeneity is introduced, such as one shown in Fig. 4, the specimen will deform as cuboid. From the vertical and horizontal specimen deformations, the homogenized Young's modulus and Poisson's ratio can be easily back-calculated as will be discussed later. More importantly, these specific boundary conditions reproduce a common experimental setup, when displacements are applied without friction on all sides of the specimen. These boundary conditions are important from a practical point of view as they allow one to compare numerical simulations with experimental results. Another advantage of these boundary conditions is that, comparing to purely static and kinematic boundary conditions, a relatively smaller RVE is required to obtain repeatable results.

To avoid memory overflow, the so-called element-by-element (EBE) method with preconditioned conjugate gradient (PCG) scheme (e.g., Smith and Griffiths, 2004) is used. The major advantage of EBE method is that it avoids assembling and storing the global stiffness matrix. In addition, since all the elements have the

---

[1] For interpretation of color in Fig. 4, the reader is referred to the web version of this article.
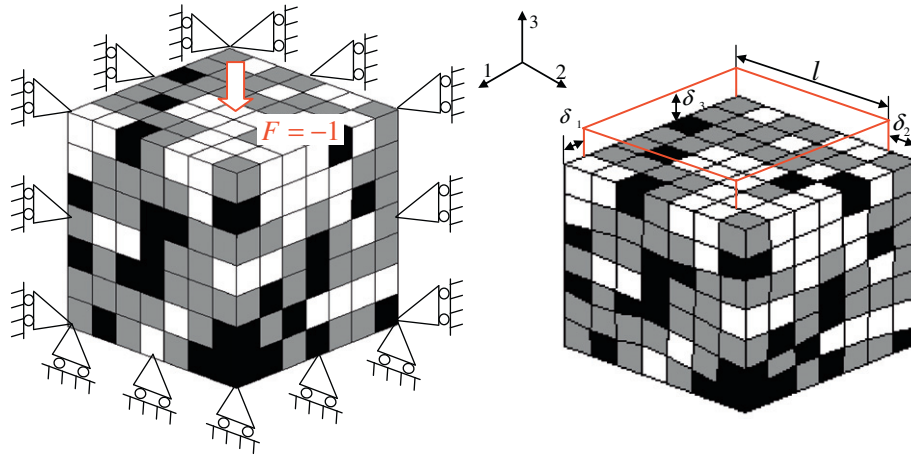
Fig. 4. FEM model and boundary conditions (left), deformed mesh (right). Rollers are placed at the bottom and the two back faces. The top and the two front faces are free but remain as planes. A unit force is applied on the top face. Dark, grey and white elements represent pores, hydrated and unhydrated cement, respectively.
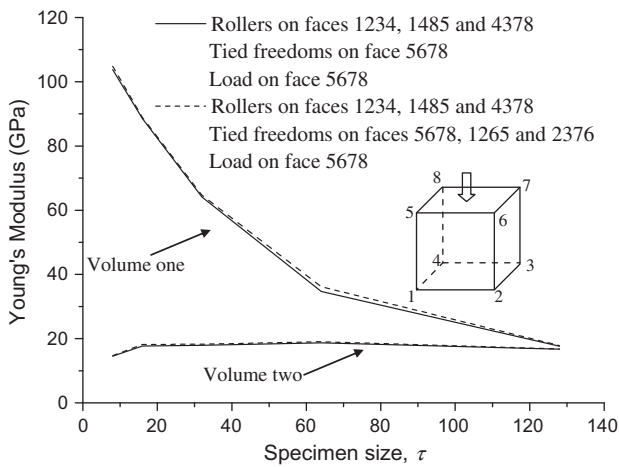

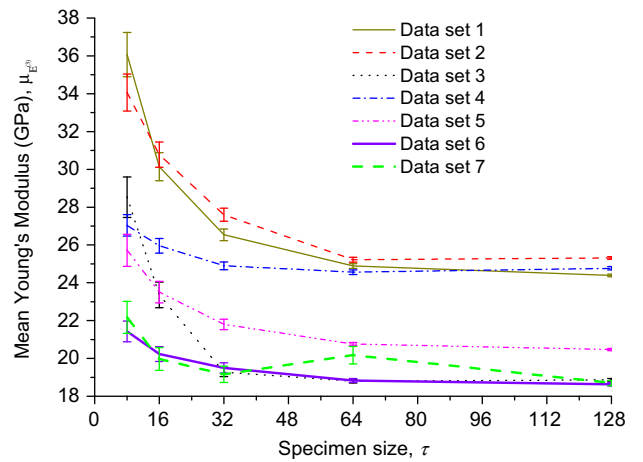**Fig. 5.** Effects of tied freedom boundary condition.

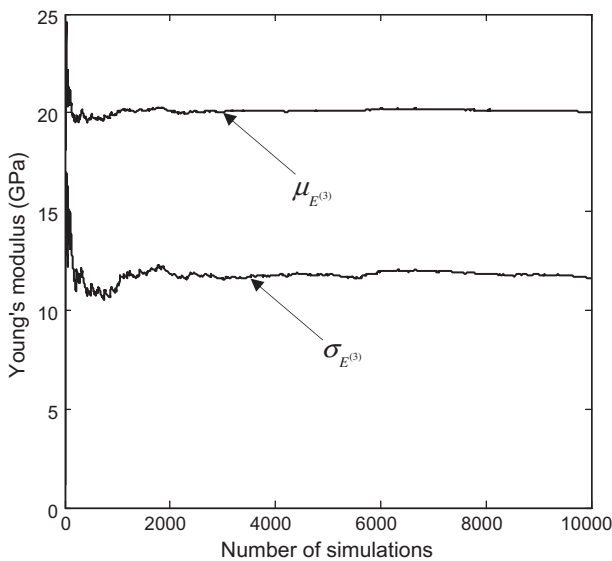**Fig. 7.** Mean homogenized Young's modulus vs. size of specimen.

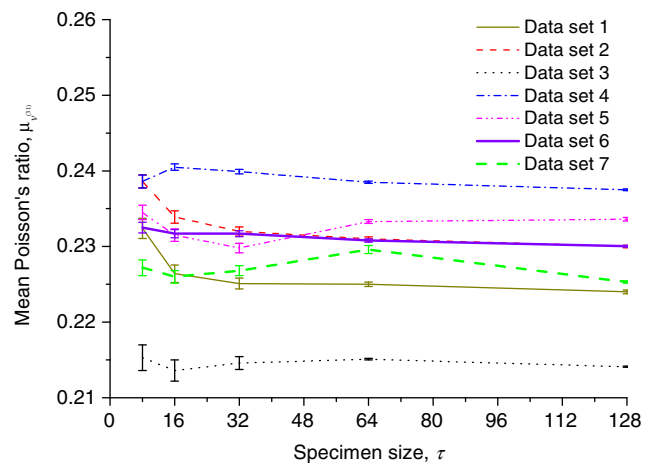**Fig. 6.** Homogenized properties vs. number of simulations.

Fig. 8. Mean homogenized Poisson's ratio vs. size of specimen.

same size and shape, the number of element stiffness matrices is reduced to the number of materials/phases. In the current study,

only three phases are considered. The element stiffness matrices can be computed and stored in memory prior to the involvement of the PCG-routine. This strategy avoids the unnecessary computation of the element stiffness matrices inside the PCG code.

Table 10
Mean homogenized properties.

Data set	τ	Load in 1			Load in 2			Load in 3		
		$\mu_{E^{(1)}}$	$\mu_{\nu^{(12)}}$	$\mu_{\nu^{(13)}}$	$\mu_{E^{(2)}}$	$\mu_{\nu^{(21)}}$	$\mu_{\nu^{(23)}}$	$\mu_{E^{(3)}}$	$\mu_{\nu^{(31)}}$	$\mu_{\nu^{(32)}}$
1	64	25.21	0.23	0.23	24.43	0.22	0.22	24.89	0.23	0.22
2	64	25.22	0.24	0.24	25.25	0.24	0.24	25.22	0.23	0.24
3	64	18.94	0.21	0.21	17.87	0.21	0.21	18.79	0.22	0.21
4	64	23.91	0.24	0.24	23.90	0.24	0.24	24.56	0.24	0.24
5	64	20.91	0.23	0.23	20.51	0.23	0.23	20.76	0.23	0.23
6	64	18.88	0.23	0.23	18.63	0.23	0.23	18.83	0.23	0.23
7	64	19.31	0.22	0.23	18.59	0.22	0.22	20.17	0.23	0.23
7	128	18.04	0.22	0.23	17.30	0.22	0.22	18.70	0.23	0.23

Table 11
Standard deviation of homogenized properties.

Data set	τ	Load in 1			Load in 2			Load in 3		
		$\sigma_{E^{(1)}}$	$\sigma_{\nu^{(12)}}$	$\sigma_{\nu^{(13)}}$	$\sigma_{E^{(2)}}$	$\sigma_{\nu^{(21)}}$	$\sigma_{\nu^{(23)}}$	$\sigma_{E^{(3)}}$	$\sigma_{\nu^{(31)}}$	$\sigma_{\nu^{(32)}}$
1	64	2.55	0.01	0.01	2.64	0.01	0.01	3.31	0.01	0.01
2	64	2.79	0.01	0.01	3.51	0.01	0.01	3.54	0.01	0.01
3	64	2.53	0.01	0.01	2.36	0.01	0.01	2.41	0.01	0.01
4	64	3.30	0.01	0.01	3.57	0.01	0.01	3.48	0.01	0.01
5	64	2.21	0.01	0.01	2.39	0.01	0.01	2.03	0.01	0.01
6	64	2.98	0.01	0.01	2.76	0.01	0.01	2.73	0.01	0.01
7	64	10.69	0.02	0.02	10.39	0.01	0.01	12.51	0.01	0.01
7	128	2.21	0.01	0.01	2.20	0.01	0.01	3.61	0.01	0.01

The finite element analysis of the RVE yields the stress and strain fields within the heterogeneous material. The corresponding average quantities can be obtained by taking a volume average Alternatively, the average strain and stress can be related to the boundary displacements and forces of the RVE by using Gauss theorem as:

$$\mathbf{E} = \langle \boldsymbol{\varepsilon}_r \rangle = \frac{1}{V} \sum_{r=1}^{n} \int_{V_r} \boldsymbol{\varepsilon}_r \, dV_r = \frac{1}{V} \int_{\Gamma} \mathbf{u}(\mathbf{x}) \cdot \mathbf{n} d\Gamma, \quad \forall \mathbf{x} \in \Omega \qquad (12)$$

$$\boldsymbol{\Sigma} = \langle \boldsymbol{\sigma}_r \rangle = \frac{1}{V} \sum_{r=1}^{n} \int_{V_r} \boldsymbol{\sigma}_r \, dV_r = \frac{1}{V} \int_{\Gamma} \mathbf{t}(\mathbf{x}) \cdot \mathbf{n} d\Gamma, \quad \forall \mathbf{x} \in \Omega \qquad (13)$$
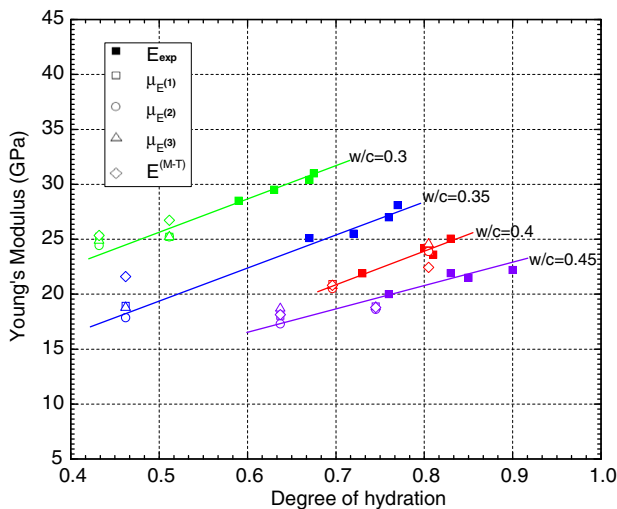

Fig. 10. Mean homogenized shear modulus compared to experimental results. G_{exp} is the experimental shear modulus obtained by Haecker et al. (2005), $G^{(\text{M-T})}$ is the analytically predicted shear modulus (Table 9), $\mu_{G^{(1)}}$, $\mu_{G^{(2)}}$ and $\mu_{G^{(3)}}$ are the mean shear modulus obtained by the numerical homogenizations loading in the directions 1, 2 and 3, respectively (Table 10).

where n is the number of phases, $\boldsymbol{\sigma}_r$ and $\boldsymbol{\varepsilon}_r$ are stress and strain tensors of phase r, V is the volume of RVE, $\mathbf{u}$ is the prescribed displacements at the boundary, $\mathbf{x}$ belongs to the boundary Ω, $\mathbf{t}$ is the traction vector, $\mathbf{n}$ is unit outward normal of the boundary, the symbol "·" stands for scalar product and $\langle \ \rangle$ denotes volume average.

Based on the load and boundary conditions shown in Fig. 4,

$$\langle \sigma_1 \rangle = \langle \sigma_2 \rangle = 0, \quad \langle \sigma_3 \rangle = -1 \qquad (14)$$

$$\langle \varepsilon_1 \rangle = \frac{\delta_1}{l}, \quad \langle \varepsilon_2 \rangle = \frac{\delta_2}{l}, \quad \langle \varepsilon_3 \rangle = \frac{-\delta_3}{l} \qquad (15)$$

where $\langle \sigma_1 \rangle$, $\langle \sigma_2 \rangle$, $\langle \sigma_3 \rangle$, $\langle \varepsilon_1 \rangle$, $\langle \varepsilon_2 \rangle$ and $\langle \varepsilon_3 \rangle$ are the volume averaged normal stresses and strains, δ_1, δ_2 and δ_3 are the specimen displacements as shown in Fig. 4, l is the side length of the RVE.

Fig. 9. Mean homogenized Young's modulus compared to experimental results. E_{exp} is the experimental Young's modulus obtained by Haecker et al. (2005), $E^{(\text{M-T})}$ is the analytically predicted Young's modulus (Table 9), $\mu_{E^{(1)}}$, $\mu_{E^{(2)}}$ and $\mu_{E^{(3)}}$ are the mean Young's modulus obtained by the numerical homogenizations loading in the directions 1, 2 and 3, respectively (Table 10).
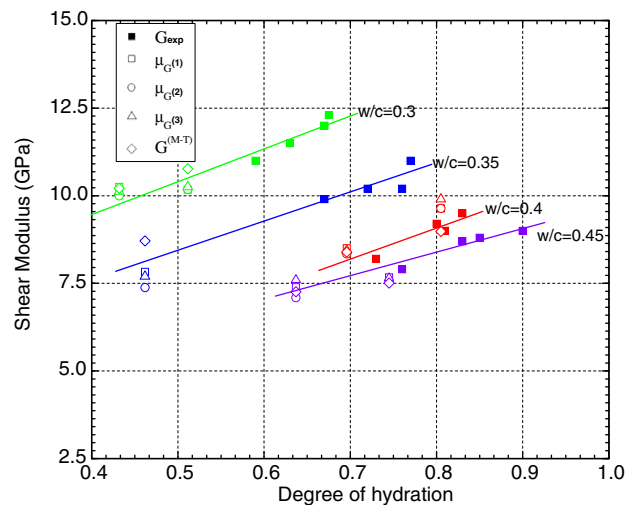
Based on the Hooke's law,

$$\langle\varepsilon_1\rangle = \frac{1}{E}[\langle\sigma_1\rangle - v(\langle\sigma_2\rangle + \langle\sigma_3\rangle)]$$

$$\langle\varepsilon_2\rangle = \frac{1}{E}[\langle\sigma_2\rangle - v(\langle\sigma_1\rangle + \langle\sigma_3\rangle)] \quad (16)$$

$$\langle\varepsilon_3\rangle = \frac{1}{E}[\langle\sigma_3\rangle - v(\langle\sigma_1\rangle + \langle\sigma_2\rangle)]$$

Substituting Eqs. (14) and (15) into (16), three parameters can be obtained,

$$E^{(3)} = \frac{1}{l\delta_3}, \quad v^{(31)} = -\frac{\delta_1}{\delta_3}, \quad v^{(32)} = -\frac{\delta_2}{\delta_3} \quad (17)$$

where $E^{(3)}$, $v^{(31)}$ and $v^{(32)}$ are the Young's modulus and Poisson's ratios obtained by loading in direction 3. The difference between $v^{(31)}$ and $v^{(32)}$ is a good indicator of anisotropy.

In order to test the assumption that cement pastes are isotropic, in addition to checking the difference between $v^{(31)}$ and $v^{(32)}$, each specimen is loaded separately in directions 1 and 2 as well. The same FEM model shown in Fig. 4 is used except that loading is applied in a different direction. The computed elastic properties are denoted as $E^{(1)}$, $v^{(12)}$ and $v^{(13)}$ for loading in direction 1, and $E^{(2)}$, $v^{(21)}$ and $v^{(23)}$ for loading in direction 2.

The effect of tied boundary conditions on the homogenized properties was first studied using data set 7 (pt045_sld_7dv1c300). Two volumes of size $\tau = 8$ were extracted randomly from the image (τ is the side length of the specimen). For each volume, two types of boundary conditions were applied. One is the proposed boundary conditions as shown in Fig. 4. Another was obtained by removing the tied freedom conditions from the two front faces (faces 1265 and 2376 in Fig. 5). Two apparent Young's moduli resulting from application of these two different boundary conditions were computed for each volume. This procedure was repeated by increasing the volume size τ with the results depicted in Fig. 5. It can be seen from this figure that introducing tied freedoms did not introduce significant constraints on the specimen.

5.2. Statistical homogenization

The statistical computational procedure used for extracting effective elastic properties follows that of a number of other authors, notably Zohdi and Wriggers (2001), Kanit et al. (2003) and Ostoja-Starzewski (2006). The basic procedure is as follows. A volume of a given size, τ, is first selected at random. The governing equations are then discretized over this volume by means of FEM, and the apparent property is computed. For each τ, this procedure is repeated N times, where N is sufficiently large for the computed statistical average to attain a constant value. Next, the volume size, τ, is increased, and the procedure is repeated until the statistical average is deemed to be independent of the volume size. The final statistical average is then taken as being the sought effective property.

In order to decide how many simulations are needed to obtain statistically repeatable results, up to 10,000 specimens ($\tau = 64$) were extracted randomly from data set 7. A FEM analysis with boundary conditions shown in Fig. 4 was conducted for each specimen. Fig. 6 shows the dependency of the mean Young's modulus ($\mu_{E^{(3)}}$) and standard deviation ($\sigma_{E^{(3)}}$) on the number of simulations. It can be seen from Fig. 6 that 2000 simulations are sufficient to give reliable and reproducible estimates of the mean Young's modulus. It is also interesting to note that the standard deviation of the Young's modulus was not reduced by increasing the number of simulations beyond 2000. It was thus decided to increase the size of specimen to see if the standard deviation can be reduced. In the reminder of this study, two thousand simulations were used.

The size effect on the mean properties was studied by changing the size of specimen in the range of {$\tau = 8, 16, 32, 64$ and 128}. The mean Young's modulus ($\mu_{E^{(3)}}$) and Poisson's ratio are shown in Figs. 7 and 8. Also shown in Figs. 7 and 8 are the 90% confidence interval based on two thousand simulations. It can be observed that for all data sets except the set No. 7, 64^3 voxels ($\tau = 64$) are sufficient to give reliable results. It is also interesting to note that the size effect can be non-monotonic as follows from plots in Fig. 7 (e.g., Huet, 1990; Kanit et al., 2003).

The mean and standard deviation of the homogenized Young's modulus and Poisson's ratio are summarized in Tables 10 and 11. Comparing the results obtained by loading the specimen in three different directions, it can be concluded that the seven considered cement pastes have isotropic elastic properties.

For data set 7 with specimen size $\tau = 64$, the coefficients of variation of Young's modulus (σ_E/μ_E) are 0.55, 0.56 and 0.62 for loading in directions 1, 2 and 3, respectively. When the size of specimen was increased to $\tau = 128$, those coefficients of variation were reduced to 0.12, 0.13 and 0.19, indicating a size of $\tau = 128$ is necessary to obtain reliable results for data set 7. Therefore, in the following, the results of data set 7 were obtained by using $\tau = 128$ unless otherwise indicated.

It can be seen that the coefficients of variation of Poisson's ratio for all 7 data sets are less than 0.1, suggesting that Poisson's ratio may be treated as a deterministic variable for the sake of simplicity (e.g., Fenton and Griffiths, 2008). The coefficients of variation of Young's modulus are less than 0.2 for all 7 data sets. The coefficients of variation of Poisson's ratio are less than the coefficients of variation of Young's modulus for all seven cement pastes. This is expected because the range of input Poisson's ratio is narrower than that of input Young's modulus as shown in Table 4.

5.3. Comparison of homogenized and experimental results

It should be noted that the Poisson's ratios obtained by applying corresponding horizontal specimen displacements are approximately the same (i.e. $v^{(12)} \approx v^{(13)}$). Hence, only one Poisson's ratio was used to calculate shear modulus for each loading direction. The mean Young's modulus and shear modulus from two thousand simulations are compared to the experimental results obtained by

Table 12
Suggested statistical elastic properties of cement paste.

Data set	w/c	α	τ	Young's modulus (GPa) 6000 simulations		Poisson's ratio 12000 simulations	
				μ_E	σ_E	μ_v	σ_v
1	0.3	0.432	64	24.84	2.87	0.23	0.009
2	0.3	0.512	64	25.23	3.30	0.24	0.007
3	0.35	0.462	64	18.53	2.48	0.21	0.012
4	0.40	0.805	64	24.13	3.47	0.24	0.005
5	0.40	0.696	64	20.73	2.22	0.23	0.007
6	0.45	0.745	64	18.78	2.83	0.23	0.007
7	0.45	0.637	128	18.02	2.81	0.22	0.010

Haecker et al. (2005) in Figs. 9 and 10. It can be seen from these figures that the results are in very good agreement. Also shown in Figs. 9 and 10 are the results obtained by analytical homogenizations (Table 9), which are in good agreement with experimental results as well.

The comparison shown in Figs. 9 and 10 suggests that by taking average of the three mean values obtained by loading in three different directions, better agreement with experimental results can be obtained. Since all seven selected cement pastes showed isotropic elastic properties, it is reasonable to treat the results obtained by loading in three different directions as independent realizations. In this way, there will be 6000 simulations for Young's modulus and 12000 simulations for Poisson's ratio. The statistical parameters from 6000 simulations of Young's modulus and 12000 simulations of Poisson's ratio are summarized in Table 12.

6. Concluding remarks

The problem of extracting statistical elastic properties of cement paste based on X-ray microtomography images has been considered. A general statistical homogenization framework is developed and applied to selected data sets. The mean homogenized elastic properties of cement pastes are in good agreement with experimental results. Since the elastic moduli estimated from analytical homogenization and the mean elastic moduli estimated from FEM compare well with each other, it could be concluded that the mean elastic properties are, in first order, mostly governed by the volume fractions of the different phases only. The numerical homogenization based on FEM provides statistically however, both the first moment (mean) and the second moment (standard deviation) of elastic moduli.

Acknowledgments

References

Arns, C.H., Knackstedt, M.A., Pinczewski, W.V., Garboczi, E.J., 2002. Computation of linear elastic properties from microtomographic images: methodology and agreement between theory and experiment. Geophysics 67 (5), 1396–1405.

Bary, B., Haha, M.B., Adam, E., Montarnal, P., 2009. Numerical and analytical effective elastic properties of degraded cement pastes. Cement and Concrete Research 39 (10), 902–912.

Bentz, D.P., 1997. Three-dimensional computer simulation of Portland cement hydration and microstructure development. Journal of the American Ceramic Society 80 (1), 3–21.

Bentz, D.P., Mizell, S., Satterfield, S., Devaney, J., George, W., Ketcham, P., Graham, J., Porterfield, J., Quenard, D., Vallee, F., Sallee, H., Boller, E., Baruchel, J., 2002. The visible cement data set. Journal of Research of the National Institute of Standards and Technology 107 (2), 137–148.

Bernard, O., Ulm, F.-J., Lemarchand, E., 2003. A multiscale micromechanics-hydration model for the early-age elastic properties of cement-based materials. Cement and Concrete Research 33 (9), 1293–1309.

Boumiz, A., Vernet, C., Tenoudji, F.C., 1996. Mechanical properties of cement pastes and mortars at early ages: evolution with time and degree of hydration. Advanced Cement Based Materials 3 (3–4), 94–106.

Chen, J.J., Sorelli, L., Vandamme, M., Ulm, F.J., Chanvillard, G., 2010. A coupled nanoindentation/SEM-EDS study on low water/cement ratio Portland cement paste: evidence for C-S-H/Ca(OH)(2) nanocomposites. Journal of the American Ceramic Society 93 (5), 1484–1493.

Constantinides, G., Ulm, F.-J., 2004. The effect of two types of C-S-H on the elasticity of cement-based materials: results from nanoindentation and micromechanical modeling. Cement and Concrete Research 34 (1), 67–80.

Eijk van, R.J., Brouwers, H.J.H., 1998. Study of the relation between hydrated Portland cement composition and leaching resistance. Cement and Concrete Research 28 (6), 815–828.

Fenton, G.A., Griffiths, D.V., 2008. In: Hoboken, N.J. (Ed.), Risk Assessment in Geotechnical Engineering. John Wiley & Sons.

Garboczi, E.J., Bullard, J.W., Bentz, D.P., 2004. Virtual testing of cement and concrete – USA 2004. Concrete International 26 (12), 33–37.

Garboczi, E.J., Day, A.R., 1995. An algorithm for computing the effective linear elastic properties of heterogeneous materials: three-dimensional results for composites with equal phase Poisson ratios. Journal of the Mechanics and Physics of Solids 43 (9), 1349–1362.

Haecker, C., Garboczi, E.J., Bullard, J.W., Bohn, R.B., Sun, Z., Shah, S.P., Voigt, T., 2005. Modeling the linear elastic properties of Portland cement paste. Cement and Concrete Research 35 (10), 1948–1960.

Hain, M., Wriggers, P., 2008. Numerical homogenization of hardened cement paste. Computational Mechanics 42 (2), 197–212.

Hazanov, S., 1998. Hill condition and overall properties of composites. Archive of Applied Mechanics 68 (6), 385–394.

Hazanov, S., Amieur, M., 1995. On overall properties of elastic heterogeneous bodies smaller than the representative volume. International Journal of Engineering Science 33 (9), 1289–1301.

Hazanov, S., Huet, C., 1994. Order relationships for boundary-conditions effect in heterogeneous bodies smaller than the representative volume. Journal of the Mechanics and Physics of Solids 42 (12), 1995–2011.

Hill, R., 1965. A self-consistent mechanics of composite materials. Journal of the Mechanics and Physics of Solids 13 (4), 213–222.

Holzer, L., Muench, B., Wegmann, M., Gasser, P., Flatt, R.J., 2006. FIB-nanotomography of particulate systems – Part I: Particle shape and topology of interfaces. Journal of the American Ceramic Society 89 (8), 2577–2585.

Huet, C., 1990. Application of variational concepts to size effects in elastic heterogeneous bodies. Journal of the Mechanics and Physics of Solids 38 (6), 813–841.

Iuga, M., Raether, F., 2007. FEM simulations of microstructure effects on thermoelastic properties of sintered ceramics. Journal of the European Ceramic Society 27 (2–3), 511–516.

Jennings, H.M., 2000. A model for the microstructure of calcium silicate hydrate in cement paste. Cement and Concrete Research 30 (1), 101–116.

Jennings, H.M., Bullard, J.W., Thomas, J.J., Andrade, J.E., Chen, J.J., Scherer, G.W., 2008. Characterization and modeling of pores and surfaces in cement paste: correlations to processing and properties. Journal of Advanced Concrete Technology 6 (1), 5–29.

Jennings, H.M., Thomas, J.J., Gevrenov, J.S., Constantinides, G., Ulm, F.-J., 2007. A multi-technique investigation of the nanoporosity of cement paste. Cement and Concrete Research 37 (3), 329–336.

Kanit, T., Forest, S., Galliet, I., Mounoury, V., Jeulin, D., 2003. Determination of the size of the representative volume element for random composites: statistical and numerical approach. International Journal of Solids and Structures 40 (13–14), 3647–3679.

Karim, M.R., Krabbenhoft, K., 2010. Extraction of effective cement paste diffusivities from X-ray microtomography scans. Transport in Porous Media 84 (2), 371–388.

Kenesei, P., Borbely, A., Biermann, H., 2004. Microstructure based three-dimensional finite element modeling of particulate reinforced metal-matrix composites. Materials Science and Engineering A – Structural Materials Properties Microstructure and Processing 387–389, 852–856.

Khisaeva, Z.F., Ostoja-Starzewski, M., 2006. On the size of RVE in finite elasticity of random composites. Journal of Elasticity 85 (2), 153–173.

Krabbenhoft, K., Hain, M., Wriggers, P., 2008. Computation of effective cement paste diffusivities from microtomographic images. Composites with Micro-and Nano-Structures: Computational Modeling and Experiments 9, 281–297.

Madadi, M., Jones, A.C., Arns, C.H., Knackstedt, M.A., 2009. 3D imaging and simulation of elastic properties of porous materials. Computing in Science & Engineering 11 (4), 65–73.

Mori, T., Tanaka, K., 1973. Average stress in matrix and average elastic energy of materials with misfitting inclusions. Acta Metallurgica 21 (5), 571–574.

Munch, B., Gasser, P., Holzer, L., Flatt, R., 2006. FIB-nanotomography of particulate systems – Part II: Particle recognition and effect of boundary truncation. Journal of the American Ceramic Society 89 (8), 2586–2595.

Ostoja-Starzewski, M., 2006. Material spatial randomness: from statistical to representative volume element. Probabilistic Engineering Mechanics 21 (2), 112–132.

Power, T.C., 1962. Physical properties of cement paste. In: Proceedings of the Fourth International Symposium on Chemistry of Cement DC, National Bureau of Standards Monograph 43, vol. 2, pp. 577–613.

Richardson, I.G., 2000. The nature of the hydration products in hardened cement pastes. Cement and Concrete Composites 22 (2), 97–113.

Sanahuja, J., Dormieux, L., Chanvillard, G., 2007. Modelling elasticity of a hydrating cement paste. Cement and Concrete Research 37 (10), 1427–1439.

Smilauer, V., Bittnar, Z., 2006. Microstructure-based micromechanical prediction of elastic properties in hydrating cement paste. Cement and Concrete Research 36 (9), 1708–1718.

Smith, I.M., Griffiths, D.V., 2004. In: Hoboken, N.J. (Ed.), Programming the Finite Element Method. Springer.

Stefan, L., Benboudjema, F., Torrenti, J.M., Bissonnette, B., 2010. Prediction of elastic properties of cement pastes at early ages. Computational Materials Science 47 (3), 775–784.

Sun, Z.H., Ye, G., Shah, S.P., 2005. Microstructure and early-age properties of Portland cement paste – effects of connectivity of solid phases. ACI Materials Journal 102 (2), 122–129.

Taylor, H.F.W., 1997. Cement Chemistry. Thomas Telford, London.

Tennis, P.D., Jennings, H.M., 2000. A model for two types of calcium silicate hydrate in the microstructure of Portland cement pastes. Cement and Concrete Research 30 (6), 855–863.

Trtik, P., Münch, B., Gasser, P., Leemann, A., Loser, R., Wepf, R., Lura, P., 2011. Focussed ion beam nanotomography reveals the 3D morphology of different solid phases in hardened cement pastes. Journal of Microscopy 241 (3), 234–242.

Trtik, P., Münch, B., Lura, P., 2009. A critical examination of statistical nanoindentation on model materials and hardened cement pastes based on virtual experiments. Cement and Concrete Composites 31 (10), 705–714.

Ulm, F.J., Vandamme, M., Bobko, C., Ortega, J.A., 2007. Statistical indentation techniques for hydrated nanocomposites: concrete, bone, and shale. Journal of the American Ceramic Society 90 (9), 2677–2692.

Wriggers, P., Hain, M., 2007. Micro–meso–macro modelling of composite materials. Computational Plasticity 7, 105–122.

Zheng, Q.S., Du, D.X., 2001. An explicit and universally applicable estimate for the effective properties of multiphase composites which accounts for inclusion distribution. Journal of the Mechanics and Physics of Solids 49 (11), 2765–2788.

Zohdi, T.I., Wriggers, P., 2001. Aspects of the computational testing of the mechanical properties of microheterogeneous material samples. International Journal for Numerical Methods in Engineering 50 (11), 2573–2599.